Pattern Formation during the Oxidation of CO on Pt{100}: A Mesoscopic Model

Rebecca B. Hoyle,[1] Alexandra T. Anghel,[2] Michael R. E. Proctor,[2] and David A. King[3]
[1]*Dept. of Mathematics, University of Surrey, Guildford, Surrey GU2 7XH, United Kingdom*
[2]*D.A.M.T.P., University of Cambridge, Wilberforce Road, Cambridge CB3 0WA, United Kingdom*
[3]*Dept. of Chemistry, University of Cambridge, Lensfield Road, Cambridge CB2 1EW, United Kingdom*
(Received 2 March 2007; published 31 May 2007)

Constantly changing irregular patterns of carbon monoxide (CO) and oxygen are seen during CO oxidation on platinum crystals in the [100] orientation. Ours is the first reaction-diffusion model to reproduce this pattern formation on physically feasible length and time scales, faithfully incorporating the available experimental data. Numerical simulations show patterns made up of CO and oxygen fronts moving at similar speeds to those seen in experiments.

DOI: 10.1103/PhysRevLett.98.226102 PACS numbers: 68.43.Bc, 68.47.De, 82.40.Ck

Spatiotemporal pattern formation occurs in a number of catalytic reactions, such as the Belousov-Zhabotinsky reaction where oscillating spirals and targets are seen [1]. Similar structures form during the catalytic oxidation of carbon monoxide on the surface of single platinum crystals, where patterns comprise areas of different surface phase or covered by different adsorbates. During the reaction, oxygen and CO are adsorbed onto the platinum surface. At high enough temperatures and for certain orientations of the surface relative to the bulk crystal, the presence of adsorbates leads to a phase change, i.e., a rearrangement of the surface platinum atoms. When the oxygen and CO react, carbon dioxide gas is released, and the surface reverts to its original configuration. This cycle can lead to kinetic oscillations in the surface phase. If communication between different areas on the crystal is very rapid compared with the rate of oscillation, the whole surface oscillates in phase; otherwise, there can be phase lags across the surface and spatial patterns arise [2]. There are two main spatial coupling mechanisms: diffusion of CO across the surface, important at low pressures, and global coupling through the gas phase, which dominates at high pressures. The surface orientation has a decisive effect on pattern formation: in the [111] orientation, there is no phase change and hence no patterns, on Pt{110} classical spirals and targets are seen (e.g., [3]), while on Pt{100}, the patterns are typically more irregular [4–6], though circular wave fronts are also seen [5].

In this Letter, we model pattern formation in CO oxidation on a single platinum crystal in the [100] orientation. The kinetic mechanism for this reaction is well established and has been modeled extensively [7–9]. Spatial modelling has concentrated on Pt{110} using a simplified representation of the kinetic mechanism, extended to include diffusion terms (and sometimes gas global coupling) [10]. These models produce results that qualitatively resemble experimentally observed patterns, but they cannot be used for detailed quantitative comparison since both the kinetic and diffusion mechanisms are simplified. Monte Carlo methods are also used, but at present, these must assume unrealistically low diffusion coefficients in order to allow pattern formation on computationally accessible length and time scales [11]. We present a mesoscopic spatial model based on the detailed kinetic mechanism [9] together with diffusion terms derived from a careful consideration of adsorbate migration on the surface. Our model allows the faithful simulation of two-dimensional pattern formation on experimental length and time scales.

The clean Pt{100} surface can be prepared in the metastable bulk-terminated 1×1 state at 300 K, with the surface atoms in a square configuration. Above 500 K, the surface restructures into the more stable hex state where the top layer of atoms is arranged hexagonally. Adsorption of CO onto the hex phase lifts the surface reconstruction, causing patches of 1×1 to form. The adsorption probability of oxygen on the hex phase is negligible. However, both oxygen and CO stick onto the 1×1 surface, where they react. They are then released in the form of CO_2 gas, and the clean 1×1 phase relaxes back into the hex state. Thus the reaction can lead to oscillations in the surface coverages of hex and 1×1 phases and adsorbates. The reaction scheme is adapted from [8,9]

$$\mathrm{CO_{gas}} + \mathrm{Pt\{100\}hex} \overset{k_1,k_2}{\Leftrightarrow} \mathrm{CO_{hex}}$$

$$\mathrm{CO_{gas}} + \mathrm{Pt\{100\}1\times 1} \overset{k_1,k_3}{\Leftrightarrow} \mathrm{CO_{1\times 1}}$$

$$\mathrm{CO_{hex}} + \mathrm{Pt\{100\}1\times 1} \overset{k_4,k_5}{\Leftrightarrow} \mathrm{CO_{1\times 1}} + \mathrm{Pt\{100\}hex}$$

$$1/2\mathrm{O_{2gas}} + \mathrm{Pt\{100\}1\times 1} \overset{k_6}{\rightarrow} \mathrm{O_{1\times 1}}$$

$$n\mathrm{CO_{hex}} + m\mathrm{Pt\{100\}hex} \overset{k_8}{\rightarrow} n\mathrm{CO_{1\times 1}} + m\mathrm{Pt\{100\}1\times 1}$$

$$\mathrm{Pt\{100\}1\times 1} \overset{k_9}{\rightarrow} \mathrm{Pt\{100\}hex}$$

$$\mathrm{CO_{1\times 1}} + \mathrm{O_{1\times 1}} \overset{k_7}{\rightarrow} \mathrm{CO_{2gas}} + 2\mathrm{Pt\{100\}1\times 1}$$

where adsorbates are denoted by subscripts hex and 1×1 and gases by gas. Adsorbed oxygen exists as single atoms in contrast to the molecular oxygen gas. The reaction rates

in ML mbar^{-1} s^{-1} are $k_1 = 2.22 \times 10^5$, $k_2 = 3.7 \times 10^{12} \exp[-105/(RT)]$, $k_5 = 10^4 \exp[-49/(RT)]$, $k_6 = 2.08 \times 10^5$, $k_7 = 2.0 \times 10^9 \exp[-58.6/(RT)]$, $k_8 = 4.9 \times 10^4$ and $k_9 = 2.5 \times 10^{11} \exp[-108/(RT)]$, where $R = 0.0083$ kJ mol^{-1} K^{-1} and T is temperature. The rates k_3 and k_4 depend on the adsorbate coverages and take the respective values $10^{15} \exp[-154/(RT)]$ and 43 in ML mbar^{-1} s^{-1} at zero coverage [9].

Experimental images distinguish between clean surface, oxygen-covered, and CO-covered areas (e.g., [6]). Accordingly, we follow pattern formation using adsorbate coverages. We write $\theta_{\rm hex}$ and $\theta_{1\times1}$ for the coverages of hex and 1×1 phases, respectively, (such that $\theta_{\rm hex} + \theta_{1\times1} = 1$), and then $\theta_{\rm CO}^{\rm hex}$, $\theta_{\rm CO}^{1\times1}$, and $\theta_{\rm O}^{1\times1}$ for the *local* adsorbate coverages on the hex and (1×1) phases. Finally, we denote by $\theta_e^{\rm hex}$ and $\theta_e^{1\times1}$ the local coverage of empty sites on the two phases, such that $\theta_{\rm CO}^{\rm hex} + \theta_e^{\rm hex} = 1$ and $\theta_{\rm CO}^{1\times1} + \theta_{\rm O}^{1\times1} + \theta_e^{1\times1} = 1$.

We extend the standard kinetic rate equations adapted from [9], to include the surface migration of CO and surface density changes at phase change, leading to the following reaction-diffusion equations:

$$\begin{aligned}
\frac{\partial(\theta_{\rm CO}^{\rm hex}\theta_{\rm hex})}{\partial t} &= k_1 p_{\rm CO} S_{\rm CO}^{\rm hex}\theta_{\rm hex}(1-\theta_{\rm CO}^{\rm hex}) - k_2\theta_{\rm CO}^{\rm hex}\theta_{\rm hex} - k_4 B\theta_{\rm CO}^{\rm hex}(1-\theta_{\rm O}^{1\times1}-\theta_{\rm CO}^{1\times1}) + k_5 B\theta_{\rm CO}^{1\times1}(1-\theta_{\rm CO}^{\rm hex}) \\
&\quad + \min\left(0, -\theta_{\rm CO}^{\rm hex}\frac{\partial\theta_{1\times1}}{\partial t}\right) + \max\left(0, -0.8\theta_{\rm CO}^{1\times1}\frac{\partial\theta_{1\times1}}{\partial t}\right) - D^{\rm hex}\theta_{\rm hex}\theta_{\rm CO}^{\rm hex}\nabla^2\theta_e^{\rm hex} - D^{\rm hex}\theta_{\rm CO}^{\rm hex}\nabla^2(\theta_{\rm hex}\theta_e^{\rm hex}) \\
&\quad + D^{\rm hex}\theta_{\rm hex}\theta_e^{\rm hex}\nabla^2\theta_{\rm CO}^{\rm hex} + D^{\rm hex}\theta_e^{\rm hex}\nabla^2(\theta_{\rm hex}\theta_{\rm CO}^{\rm hex}), \\
\frac{\partial(\theta_{\rm CO}^{1\times1}\theta_{1\times1})}{\partial t} &= k_1 p_{\rm CO} S_{\rm CO}^{1\times1}\theta_{1\times1}(1-\theta_{\rm O}^{1\times1}-\theta_{\rm CO}^{1\times1}) - k_3\theta_{\rm CO}^{1\times1}\theta_{1\times1} - k_7\theta_{\rm CO}^{1\times1}\theta_{\rm O}^{1\times1}\theta_{1\times1} + k_4 B\theta_{\rm CO}^{\rm hex}(1-\theta_{\rm O}^{1\times1}-\theta_{\rm CO}^{1\times1}) \\
&\quad - k_5 B\theta_{\rm CO}^{1\times1}(1-\theta_{\rm CO}^{\rm hex}) + \max\left(0, 1.25\theta_{\rm CO}^{\rm hex}\frac{\partial\theta_{1\times1}}{\partial t}\right) + \min\left(0, \theta_{\rm CO}^{1\times1}\frac{\partial\theta_{1\times1}}{\partial t}\right) - D^{1\times1}\theta_{1\times1}\theta_{\rm CO}^{1\times1}\nabla^2\theta_e^{1\times1} \\
&\quad - D^{1\times1}\theta_{\rm CO}^{1\times1}\nabla^2(\theta_{1\times1}\theta_e^{1\times1}) + D^{1\times1}\theta_{1\times1}\theta_e^{1\times1}\nabla^2\theta_{\rm CO}^{1\times1} + D^{1\times1}\theta_e^{1\times1}\nabla^2(\theta_{1\times1}\theta_{\rm CO}^{1\times1}), \\
\frac{\partial(\theta_{\rm O}^{1\times1}\theta_{1\times1})}{\partial t} &= k_6 p_{\rm O_2} S_{\rm O_2}^{1\times1}\theta_{1\times1}(1-\theta_{\rm O}^{1\times1}-\theta_{\rm CO}^{1\times1}) - k_7\theta_{\rm CO}^{1\times1}\theta_{\rm O}^{1\times1}\theta_{1\times1} + \min\left(0, \theta_{\rm O}^{1\times1}\frac{\partial\theta_{1\times1}}{\partial t}\right), \\
\frac{\partial\theta_{1\times1}}{\partial t} &= \frac{1}{2}[k_8(\theta_{\rm O}^{\rm hex})^n\theta_{\rm hex} - k_9(1-c(\theta))\theta_{1\times1}] - \frac{1}{2}[k_8(\theta_{\rm CO}^{\rm hex})^n\theta_{\rm hex} + k_9(1-c(\theta))\theta_{1\times1}]\tanh[\kappa(1-c(\theta))],
\end{aligned}$$

where $c(\theta) = \theta_{\rm CO}^{1\times1}/0.25 + \theta_{\rm O}^{1\times1}/0.4$, $n = 4.17$, $\kappa = 1000$, $p_{\rm CO}$, and $p_{\rm O_2}$ are the partial pressures of CO and O_2, respectively, $S_{\rm CO}^{\rm hex}$ (=0.78) and $S_{\rm CO}^{1\times1}$ (=0.91 at $\theta = 0$) are the sticking probabilities of CO on hex and 1×1 phases, $S_{\rm O_2}^{1\times1}$ (=0.31 at $\theta = 0$) is the sticking probability of O_2 on 1×1 phase, and $B = 1$ measures the boundary length between the two phases [9]. (For $S_{\rm O_2}^{1\times1}$, we use the values given in [9] for recently vacated adsorption sites, and neglect a distinction between these and fully relaxed 1×1 sites.) We do not include gas global coupling in our model, since the effect is insignificant at the low pressures we consider here [6,12,13].

At phase change, about 20% of atoms are displaced [14], so a surface Pt atom in 1×1 phase occupies an area about 1.25 times that of a hex phase atom. The max and min terms in the equations account for these surface density changes at both phase change and relaxation and for the resulting displacement of adsorbed CO and oxygen.

Diffusion of CO within 1×1 and hex patches dominates over cross-phase diffusion which can only occur at phase boundaries. The diffusion rate depends not only on the density of CO in the area from which it leaves, but also on the empty site density where it arrives. The diffusion terms take account of both these observations. $D^{\rm hex}$ and $D^{1\times1}$ are half the diffusion coefficients for CO on clean hex and 1×1 phases; we set them both to be 10^{-6} cm^2 s^{-1} [4]. At the temperatures we consider, oxygen is essentially immobile.

We simulate two-dimensional (2D) pattern formation on a single 600 μm $\times$ 600 μm Pt{100} crystal, dividing the surface into a grid of 100×100 cells. Each cell contains many CO adsorption sites and is larger than the initial size of hex and 1×1 phase patches, but smaller than the characteristic length scale for pattern formation, thus, our model is mesoscopic. We also perform one-dimensional (1D) integrations on a 6 μm $\times$ 600 μm ribbon divided lengthwise into 100 cells in the spirit of [15] (but now with a faithful description of the dominant spatial coupling). We integrate the reaction-diffusion equations numerically using Adams-Bashforth time stepping and second-order spatial finite differences with periodic boundary conditions.

Figure 1 summarizes the results of 1D simulations for 10^{-6} mbar $\le p_{\rm CO} \le 10^{-5}$ mbar, 10^{-5} mbar $\le p_{\rm O_2} \le 10^{-4}$ mbar at fixed $T = 480$ K. We start with a clean surface, predominantly in hex phase, where $(\theta_{1\times1}, \theta_{\rm O}^{1\times1}, \theta_{\rm CO}^{1\times1}, \theta_{\rm CO}^{\rm hex}) = (0.001, 0, 0, 0)$, punctuated by defects where $(\theta_{\rm CO}^{1\times1}, \theta_{\rm CO}^{\rm hex}) = (0, 0)$ and $(\theta_{\rm O}^{1\times1}, \theta_{1\times1}) = (0.5, 0.5)$, (1.0,0.5), (0.5,0.9), and (1.0,0.9) in cells 1, 38, 56, and 89. The defects represent areas in 1×1 phase and partially

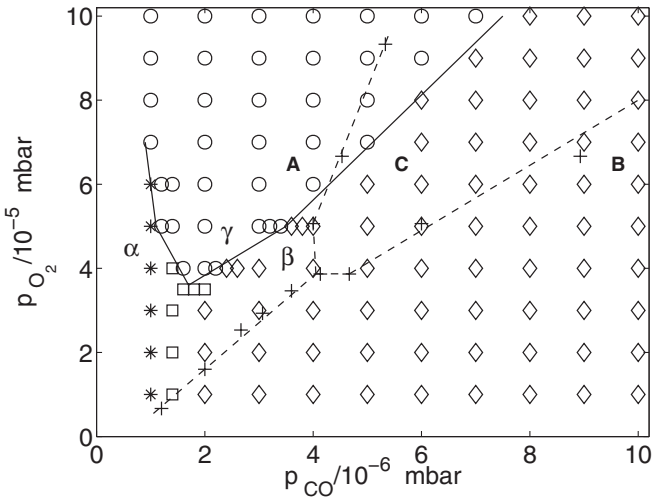

FIG. 1. The oscillation regime for our model (*, □, ◇, ○, and solid lines) is compared to that observed in experiment [12] (+ and dashed lines). Key: */□/◇ steady evolution to low/medium/high CO state; ○ regular surface oscillations. Regions α, β and γ show low and high CO and 1×1 coverages and oscillations, respectively, in simulations. Experimental regions A, B, and C [12] correspond to low and high CO coverage and oscillations, respectively.

covered by adsorbed oxygen, inspired by experiments [12] where p_{O_2} was set first and then p_{CO} increased stepwise. Each simulation was run for 1000 s.

The experimental parameter range for oscillations was mapped for varying (p_{O_2}, p_{CO}) at constant $T = 480$ K [12], revealing three distinct regions of phase space (Fig. 1). Observed oscillations are mainly irregular [6,13,16], suggesting that they are not in phase across the whole surface, and so that spatial patterns may be present. Our simulations also divide (p_{O_2}, p_{CO}) space into three regions (Fig. 1): low (region α) and high (region β) CO coverage and oscillations (region γ). In region α (β), representative values of 1×1, total CO ($\theta_{CO}^{tot} \equiv \theta_{1\times1}\theta_{CO}^{1\times1} + \theta_{hex}\theta_{CO}^{hex}$), and total oxygen ($\theta_{O}^{tot} \equiv \theta_{1\times1}\theta_{O}^{1\times1}$) coverages are 0.31, 0.13, and 4.9×10^{-5} (0.98, 0.41, and 1.4×10^{-4}). Regions α and β merge below region γ via intermediate θ_{CO}^{tot} solutions. However, a significant difference remains between the two regions, with high CO solutions developing much faster than those at low θ_{CO}^{tot}.

Both model (γ) and experimental (C) oscillatory regions are V-shaped and tilted towards higher p_{CO}. However, region γ lies at lower p_{CO} than region C. The simulations start with p_{CO} and p_{O_2} at their target values, whereas experimentally [12] p_{CO} was increased stepwise, giving a lower average value, which might explain the offset. Our oscillations have periods $P \gtrsim 80$ s, being shorter in the midrange of p_{CO} and for higher p_{O_2}. Experimentally, a decrease in p_{CO} and T increases the oscillation period [13]. In Fig. 1, we find 90 s $\lesssim P \lesssim$ 970 s, comparing well with experiments (typically at higher partial pressures), where periods lie in the range 1–4 min for work function oscillations with amplitudes 100–300 mV at $T \approx 500$ K and up to 10 mins or more at lower temperatures [13]. However, using different initial conditions and longer runs, we found periods of up to 2700 s. With small amplitudes, faster oscillations with periods of only a few seconds were found experimentally [13].

Further simulations revealed that bulk initial conditions affect the long-term surface state and can alter the positions of regions α, β, and γ: low initial CO coverage shifts the boundaries towards higher p_{CO} and vice versa. The boundaries of experimental region C were confirmed by repeatedly increasing and decreasing p_{CO}: the error bars (not shown in Fig. 1) are quite large, echoing our finding.

We find two types of propagating front: CO and oxygen-CO. CO fronts appear for the full (p_{O_2}, p_{CO}) range, at the beginning of simulations with low $\theta_{1\times1}$, $\theta_{O}^{1\times1}$, θ_{CO}^{hex} and medium/high $\theta_{CO}^{1\times1}$ defects in initially high $\theta_{1\times1}$ bulk coverages. To measure their speeds to 10% accuracy we had to use finer 200×200 or 200×1 grids. In Fig. 2, the surface initially has high $\theta_{1\times1}$ coverage and high θ_{O}^{tot} develops immediately, with θ_{CO}^{tot} insignificant. A wave of CO spreads from the defects pushing out the oxygen ahead. Phase relaxation occurs at the leading edge, shown in the sharp transition between high and low $\theta_{1\times1}$, so hex phase dominates behind the front, with θ_{CO}^{tot} remaining low and θ_{O}^{tot} negligible. For higher p_{CO} and lower p_{O_2}, θ_{O}^{tot} ahead of the front is lower and $\theta_{1\times1}$ and θ_{CO}^{tot} behind it are higher, so there is less phase relaxation. The speeds of 1D front are 0.13–14 μm s^{-1} compared with 2–50 μm s^{-1} in experiments (at higher partial pressures and for 420 K $\leq T \leq$ 540 K) [4,6]. CO fronts are slower at higher p_{O_2} and lower p_{CO} where the phase change is most marked, in accord with the argument [6] that the phase transition slows them.

We also find initial travelling reaction waves triggered by defects and consisting of an oxygen front closely fol-

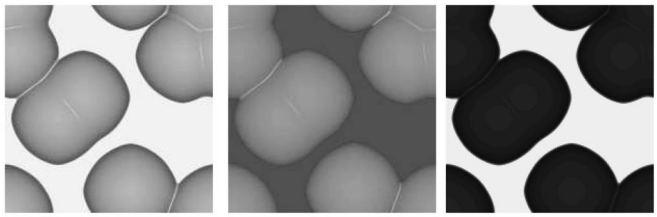

(a) (b) (c)

FIG. 2. CO front propagation in 2D at $t = 500$ s: (a) $\theta_{1\times1}$, (b) θ_{CO}^{tot}, and (c) θ_{O}^{tot} (white = 1, black = 0) at (p_{O_2}, p_{CO}) = (6×10^{-5}, 1×10^{-6}) mbar for bulk initial conditions ($\theta_{1\times1}$, $\theta_{O}^{1\times1}$, $\theta_{CO}^{1\times1}$, θ_{CO}^{hex}) = ($0.735, 2.98 \times 10^{-4}, 0.402, 3.54 \times 10^{-2}$) and 2×2 cell defects with ($\theta_{O}^{1\times1}$, $\theta_{CO}^{1\times1}$, θ_{CO}^{hex}) = ($1.10 \times 10^{-3}, 0.341, 1.98 \times 10^{-2}$) and $\theta_{1\times1} = 0.134$, 0.234, 0.334, 0.134, 0.234, 0.334 with bottom left corners at (1,1), (75, 111), (51,91), (121,21), (171, 151), and (7,155), respectively, on a 200×200 grid. The initial front speed is 0.24 μm s^{-1}.

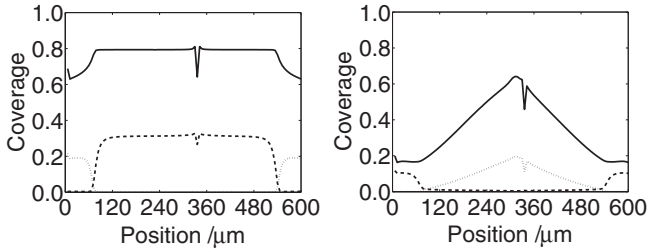

FIG. 3. 1D oxygen-CO front at $(p_{O_2}, p_{CO}) = (7 \times 10^{-5}, 3 \times 10^{-6})$ mbar : $\theta_{1\times1}$ (solid line), θ_{CO}^{tot} (dashed line), and θ_{O}^{tot} (dotted line) at times (a) 82 s and (b) 90 s, for bulk initial conditions $(\theta_{1\times1}, \theta_{O}^{1\times1}, \theta_{CO}^{1\times1}, \theta_{CO}^{hex}) = (0.735, 2.98 \times 10^{-4}, 0.402, 3.54 \times 10^{-2})$ and defects with $(\theta_{O}^{1\times1}, \theta_{CO}^{1\times1}, \theta_{CO}^{hex}) = (1.10 \times 10^{-3}, 0.341, 1.98 \times 10^{-2})$ and $\theta_{1\times1} = 0.834$, 0.734, and 0.234 in cells 1, 38, and 56, respectively. The oxygen (CO) front speed is 37(36) $\mu m\,s^{-1}$.

lowed by a CO front. For high p_{O_2}, they occur on the left-hand side of region γ, while for lower p_{O_2}, they can be found on either side and also in region α, depending on the initial conditions. The fronts are faster where the period of the ensuing oscillations is shorter. The presence of a travelling wave component in many of our oscillatory solutions fits with the observation that oscillations are typically irregular [6,13,16]. A 1D front is shown in Fig. 3: an initial solution with high $\theta_{1\times1}$, medium θ_{CO}^{tot}, and very low θ_{O}^{tot} [Fig. 3(a)] is invaded by oxygen pushing in from the sides. The adsorbed CO is removed as the reaction wave passes, and $\theta_{1\times1}$ falls. A few seconds later [Fig. 3(b)], a CO front follows, squeezing out the oxygen and priming the surface to recover to its initial state. Phase relaxation occurs at the front, but $\theta_{1\times1}$ falls less far than for CO fronts, so the oxygen-CO fronts move faster [6]. Similar consecutive waves, but with oxygen following CO, have been observed ([6] Fig. 3). Our front speeds are 13–90 $\mu m\,s^{-1}$, compared with measured oxygen front speeds of 50–500 $\mu m\,s^{-1}$ [5,6] (for higher partial pressures and 380 K $\leq T \leq$ 540 K).

In conclusion, our reaction-diffusion model successfully captures pattern formation in this system on experimental length and time scales, with numerical simulations showing moving fronts of adsorbed carbon monoxide and oxygen similar to those observed experimentally and at comparable speeds.

We thank Isabel M. Irurzun for the use of her numerical code, from which we adapted our own. This work was supported by the Leverhulme Trust.

[1] B. P. Belousov, *Sbornik Referatov po Radiatsionnoî Meditsine za 1958 god* (Medgiz, Moscow, 1958), p. 145; A. Zaikin and A. M. Zhabotinsky, Nature (London) **225**, 535 (1970).
[2] G. Ertl, Surf. Sci. **287**, 1 (1993).
[3] S. Nettesheim, A. von Oertzen, H. H. Rotermund, and G. Ertl, J. Chem. Phys. **98**, 9977 (1993).
[4] H. H. Rotermund, S. Jakubith, A. von Oertzen, and G. Ertl, J. Chem. Phys. **91**, 4942 (1989).
[5] H. H. Rotermund, W. Engel, M. Kordesch, and G. Ertl, Nature (London) **343**, 355 (1990).
[6] T. Lele and J. Lauterbach, Chaos **12**, 164 (2002).
[7] R. Imbihl, M. P. Cox, and G. Ertl, J. Chem. Phys. **83**, 1578 (1985).
[8] A. Hopkinson and D. A. King, Faraday Discuss. **96**, 255 (1993); Chem. Phys. **177**, 433 (1993); A. Hopkinson, X.-C. Guo, J. M. Bradley, and D. A. King, J. Chem. Phys. **99**, 8262 (1993); A. Hopkinson, J. M. Bradley, X.-C. Guo, and D. A. King, Phys. Rev. Lett. **71**, 1597 (1993); D. A. King, Surf. Rev. Lett. **1**, 435 (1994); M. Gruyters, T. Ali, and D. A. King, J. Phys. Chem. **100**, 14417 (1996); A. T. Pasteur, X.-C. Guo, T. Ali, M. Gruyters, and D. A. King, Surf. Sci. **366**, 564 (1996); M. Gruyters and D. A. King, J. Chem. Soc., Faraday Trans. **93**, 2947 (1997).
[9] M. Gruyters, T. Ali, and D. A. King, Chem. Phys. Lett. **232**, 1 (1995).
[10] K. Krischer, M. Eiswirth, and G. Ertl, J. Chem. Phys. **96**, 9161 (1992); A. von Oertzen, H. H. Rotermund, A. S. Mikhailov, and G. Ertl, J. Phys. Chem. B **104**, 3155 (2000); M. Falcke and H. Engel, J. Chem. Phys. **101**, 6255 (1994); Phys. Rev. E **50**, 1353 (1994); **56**, 635 (1997); M. Kim, M. Bertram, M. Pollmann, A. von Oertzen, A. S. Mikhailov, H. H. Rotermund, and G. Ertl, Science **292**, 1357 (2001).
[11] V. P. Zhdanov, Phys. Rev. E **60**, 7554 (1999); Surf. Sci. **426**, 345 (1999); V. P. Zhdanov and B. Kasemo, Phys. Rev. E **61**, R2184 (2000).
[12] M. Eiswirth, R. Schwankner, and G. Ertl, Z. Phys. Chem. Neue Folge **144**, 59 (1985).
[13] R. Imbihl, M. P. Cox, and G. Ertl, J. Chem. Phys. **84**, 3519 (1986).
[14] P. van Beurden, B. S. Bunnik, G. J. Kramer, and A. Borg, Phys. Rev. Lett. **90**, 066106 (2003).
[15] I. M. Irurzun, R. B. Hoyle, M. R. E. Proctor, and D. A. King, Chem. Phys. Lett. **377**, 269 (2003).
[16] M. P. Cox, G. Ertl, and R. Imbihl, Phys. Rev. Lett. **54**, 1725 (1985).